POLITECNICO
MILANO 1863

SCUOLA DI INGEGNERIA INDUSTRIALE
E DELL'INFORMAZIONE

Executive Summary of the Thesis

Strain Engineering in WSe_2 monolayer for Single Photon Emission

Laurea Magistrale in Materials Engineering and Nanotechnology - Ingegneria dei Materiali e Nanotecnologie

Author: Thomas Fantin

Advisor: Prof. Carlo Spartaco Casari

Co-advisor: Pablo Hernandez Lopez and Dr. Sebastian Heeg

Academic year: 2024-2025

1. Theoretical background

Transition metal dichalcogenides (TMDs) are layered materials with chemical formula MX_2, where M is a transition metal (e.g., Mo, W) and X is a chalcogen (S, Se, or Te). Each layer consists of a hexagonal plane of metal atoms sandwiched between two planes of chalcogen atoms, forming a covalently bonded monolayer. Adjacent layers are held together by van der Waals interactions, enabling mechanical exfoliation down to the monolayer limit [5].

1.1. Optical properties of Monolayer TMDs

The electronic band structure of TMDs strongly depend on thickness. Bulk TMDs typically exhibit an indirect bandgap, whereas monolayer of all the TMDs listed above, including WSe_2, become direct-gap semiconductors. In monolayer WSe_2, both the conduction band minimum and valence band maximum are located at the K and K′ points of the Brillouin zone, resulting in efficient optical emission [5].
Optical properties of monolayer TMDs are dominated by excitonic effects due to their high binding energies of hundreds of meV, related to reduced dielectric screening and strong Coulomb interactions. The photoluminescence (PL) spectrum at room temperature is primarily governed by neutral excitons and trions, i.e. excitons involving three charges, depending on the doping [5].
Strong spin–orbit coupling (SOC), particularly in tungsten-based TMDs, lifts the spin degeneracy of the valence band and gives rise to dark bands and excitonic states. Dark excitons corresponding to either spin-forbidden or valley-forbidden transitions lie energetically below bright excitons in WSe_2.
In addition, lattice defects and impurities can introduce localized interband states [5].
In TMD heterostructures, interlayer coupling leads to new electronic and optical phenomena. In systems such as WSe_2/MoS_2, type-II band alignment promotes charge separation between layers and enables the formation of interlayer excitons, where electrons and holes reside in different materials.

1.1.1 Characterization of TMDs

In unstrained monolayer WSe_2, the room-temperature PL spectrum is dominated by the emissions sum of neutral exciton and trion, and has intensity maxima at 1.65 eV.

For what concerns MoS_2 PL, in the monolayer limit the optical emission is dominated by the direct K–K transition at approximately 1.87 eV. With increasing thickness, an additional indirect transition between the Γ point in the valence band and the Q point in the conduction band emerges at 1.6 eV. This indirect Γ–Q transition progressively shifts to lower energies as the number of layers increases.
Raman spectroscopy provides a reliable method for determining the thickness of MoS_2 flakes, which is fundamental to carry out the results discussed in Section 3.1. The characteristic in-plane E_{2g} and out-of-plane A_{1g} vibrational modes shift with the number of layers. In particular, the spectral separation between these modes increases monotonically with thickness, enabling accurate layer-number identification when compared to reference samples.

1.2. Dependency of WSe_2 Photoluminescence on External Parameters

Single–photon emission (SPE) in monolayer WSe_2 is known to occur at cryogenic temperatures (typically below 10 K) and in the presence of locally induced strain.

1.2.1 Temperature Dependency

With increasing temperature, the PL emission of WSe_2 exhibits thermal broadening due to enhanced exciton–phonon interactions, accompanied by a redshift of the emission energy resulting from bandgap renormalization. At lower temperatures, linewidth narrowing occurs and also additional spectral features become distinguishable as the population distribution of electronic states changes with the temperature. These include emissions associated with trions, dark excitons, and defect-bound excitons.

1.2.2 Effect of Tensile Strain

Tensile strain reduces the bandgap, leading to a redshift of the PL emission [2]. Spatially non-uniform strain creates local energy minima within electronic bands that drive exciton funneling toward highly strained regions, resulting in enhanced local emission.
Furthermore, strain-induced lowering of the bandgap can induce hybridization between valley–dark neutral exciton state and defect–related states, at 1% and 2.5% strain approximately [2]. This results in avoided crossing of the hybridized states, which partially overcome SOC optical selection rules and activating radiative recombination channels that are forbidden in unstrained monolayers [2]. As ongoing research suggests, enhanced emission related to such hybridization would be compatible with the high oscillator strength showed in SPE.

1.3. Single-Photon Emission in WSe_2 Monolayers

Single-photon emission (SPE) represents a key resource for quantum photonics. Single–photon sources for quantum computing should be able to generate photons that are identical in all relevant degrees of freedom, namely polarization, spectral shape, temporal mode shape and spatial mode shape. The performance of single-photon sources is commonly evaluated in terms of single-photon purity (i.e. which is the probability that photons are emitted one by one), photon indistinguishability, and brightness.
In WSe_2 monolayers, SPE is typically observed at cryogenic temperatures and is often associated with localized strain or defects. A widely discussed hypothesis attributes SPE in WSe_2 to strain-induced hybridization between dark excitons and defect-related states, discussed in Paragraph 1.2.2. In this picture, such hybridization enables radiative recombination from otherwise optically forbidden states, giving rise to narrow emission lines with single-photon characteristics [4].

1.3.1 Nanobubble-induced strain for SPE in WSe_2 monolayers

Nanobubble-induced strain provides an effective route to generate localized tensile strain in WSe_2 monolayers through out-of-plane deformation caused by trapped contaminants. The resulting non-uniform strain landscape creates local bandgap minima that promote exciton funneling and localization. In the samples investigated in this work, multilayer MoS_2 is employed as a substrate primarily to quench the photoluminescence of unstrained WSe_2 regions via type-II band alignment, thereby enabling selective optical probing of strained sites. Experimental results of this work show that the strain magnitude within nanobubbles depends on the

thickness of the underlying MoS_2 substrate, an effect attributed to changes in adhesion forces that modify bubbles shape.

2. Materials and Methods

The target samples consist of WSe_2 monolayers stacked on multilayer MoS_2 substrates, where localized strain is introduced via contaminant-induced nanobubbles formed at the interface.

2.1. Sample Fabrication

Monolayer WSe_2 and multilayer MoS_2 flakes were obtained by mechanical exfoliation directly from bulk crystals, and placed onto polydimethylsiloxane (PDMS) stamps. WSe_2 monolayers were first exfoliated onto PDMS using adhesive tape, and subsequently transferred onto MoS_2 substrates with thickness ranging from one to five layers. The MoS_2 flakes could be exfoliated directly onto 0.17 mm thick glass coverslips by applying the standard scotch tape to the coverslip, and by heating at 120°C for 120 seconds. Alternatively, they could be exfoliated on PDMS and transferred onto such coverslips prior to stacking.
The WSe_2/MoS_2 stacks were assembled using a dry-transfer technique involving a motorized transfer system inside a glovebox under N_2 environment. Following assembly, the stacks were annealed in the same N_2 environment at 200°C for 12 hours approximately. This thermal treatment promotes the aggregation of interfacial contaminants into localized nanobubbles, inducing out-of-plane deformation of the WSe_2 monolayer and generating localized tensile strain.

2.2. Sample Characterization

After the annealing step the samples were characterized using the following techniques.

2.2.1 Atomic Force Microscopy

Atomic force microscopy (AFM) measurements were carried out performing the scan in AC tapping mode providing Angstrom–scale resolution.

2.2.2 Confocal spectroscopy methods

Room-temperature photoluminescence (PL) and Raman spectroscopy were performed using the same spectroscopy setup, namely XploRA Plus by Horiba. Excitation was provided either by 532, 638 or 765 nm laser focused through a high-numerical-aperture objective (NA = 0.9). Low-temperature PL measurements were instead performed in a custom–built setup, involving a continuous-flow cryostat with optical access. Within such cryostat, a liquid helium transfer line could exchange heat with an heat exchanger to which the sample wa thermally connected, allowing cooling down up to 15 K.

2.2.3 Tip-Enhanced Photoluminescence (TEPL)

Tip-enhanced photoluminescence combines scanning probe microscopy with optical spectroscopy to achieve spatial resolution beyond the diffraction limit. A metallic AFM tip acts as a nanoscale optical antenna, and when is illuminated by a focused laser beam, localized surface plasmons are excited at the tip apex, leading to strong confinement and enhancement of the electromagnetic field in a nanometric volume beneath the tip.
TEPL measurements in this work were performed using the Porto setup by FabNS, in bottom–illumination geometry. The excitation laser at 633 nm was focused through the transparent substrate, while the metallic PTTP tip by FabNS was positioned in close proximity to the sample surface. The enhancement is highly localized at the tip apex, enabling PL mapping with spatial resolution up to 10 nm.
TEPL mapping was employed to measure local PL redshift within WSe2 nanobubbles, providing nanoscale information on strain distribution, and thus the strain range present in a bubble. This technique is central to this work, as it enables strain characterization with nanometric resolution of the same nanobubbles that were then measured in the cryostat at low temperatures.
This allowed direct comparison between strain magnitude present in a bubble at room temperature and the optical behavior of the blister at cryogenic temperatures.

3. Strain engineering of nanobubbles

The spatial distribution, morphology, strain and consequently optical properties of the nanobubbles were found to be dependent on fabrication

parameters like substrate thickness and pre–stacking laser writing on the flakes.

3.1. Strain dependency on the substrate

With the purpose of studying the dependency of the strain induced in the nanobubble on the substrate thickness, the number of layers of the MoS_2 substrate in each sample was determined through a combination of PL, and Raman spectroscopy, analyzing the spectral features discussed in Paragraph 1.1.1. AFM step–height measurements also were involved in such characterization. Nanobubbles formed at the interface between WSe_2 monolayers and MoS_2 substrates were identified by correlating PL maps with AFM measurements.

The redshift of the WSe_2 PL emission in correspondence of bubbles position was interpreted as a direct signature of tensile strain. Using a gauge factor of 100 meV/% to convert the excitonic redshift into strain values, the average redshift associated with nanobubbles was plotted as a function of the MoS_2 substrate thickness. This analysis reveals that the induced strain increases with the number of MoS_2 layers and saturates for substrates consisting of four or more layers at 110 meV approximately, as reported by the red plot in Fig.1-a.

According to Sanchez et al [3], larger strain in bubbles can arise from stronger adhesion between the monolayer and the substrate, as increased interfacial forces modify the bubble shape. In the analyzed samples, the substrate thickness was found to influence nanobubble morphology (Fig.1-b). For thicker MoS_2 substrates (3-5L), nanobubbles appear more isolated and exhibit a rounded, symmetric shape, whereas on thinner substrates (1-2L) they tend to form interconnected networks with more irregular geometries.

Björkmann et al. [1] investigated the adhesion energy between a MoS_2 monolayer and MoS_2 substrates of varying thickness, showing that the energy per unit area required to exfoliate the monolayer (E_{XF}) increases monotonically with the number of layers in the substrate (N), and saturates for four or more layers. Their study is not specifically on the adhesion between WSe_2 monolayers on MoS_2 substrates, but the similarity between the $E_{XF}(N)$ trend (Fig.1-a in cyan) and the observed redshift dependence suggests that substrate-induced changes in adhesion forces play a key role in determining nanobubbles shape. Consequently, the local strain distribution (i.e. the PL emission spectrum) of individual bubbles is tuned by the substrate thickness (Fig.1-c).

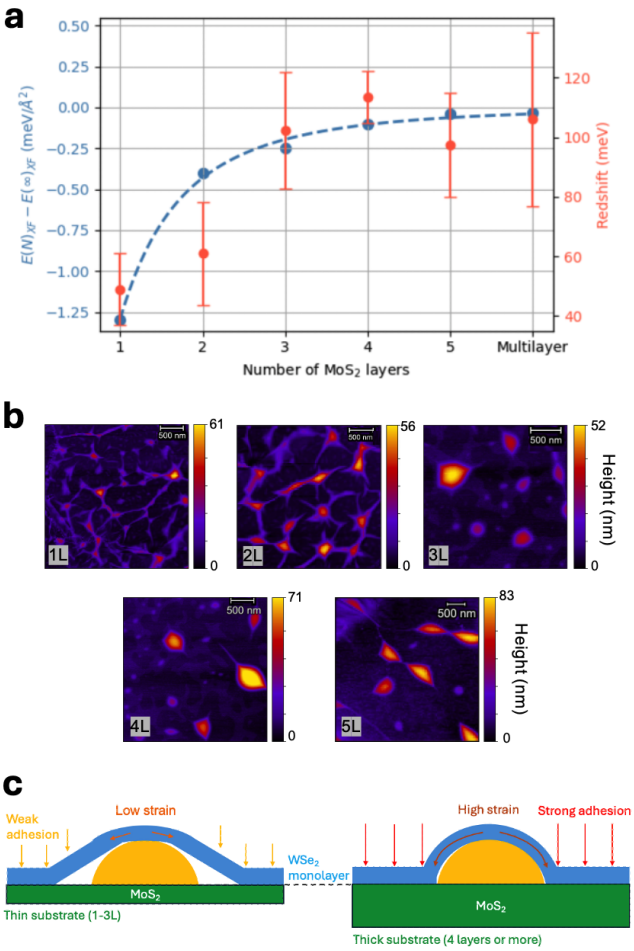

Figure 1: **Bubble strain and shape dependency on MoS_2 substrate thickness.** (a) The average induced redshift in nanobubbles for each substrate thickness is plotted in red. In cyan is plotted the energy per unit area required to exfoliate a monolayer of MoS_2 from a substrate formed by N layers of MoS_2 ($E_{XF}(N)$), subtracted to the energy required to exfoliate the monolayer form the bulk ($E_{XF}(\infty)$) [1]. Both plots follow increasing trends, saturating for four or more layers. (b) AFM maps extracted from samples having different substrate thicknesses (1-5L). (c) Representation of how the substrate thickness is expected to tune the strain induced in nanobubbles as adhesion forces vary.

3.2. Nanobubble patterning

The investigation of nanobubble patterning originated from the observation of an ordered array of nanobubbles in a sample obtained unintentionally (Fig.2-a). The bubbles were arranged on a regular square lattice with a spacing of 1 µm along both in-plane directions (Fig.2-b,c). This regularity suggested that the pattern originated from an unintended laser writing process occurring during optical characterization of the flakes while they were still supported on PDMS.

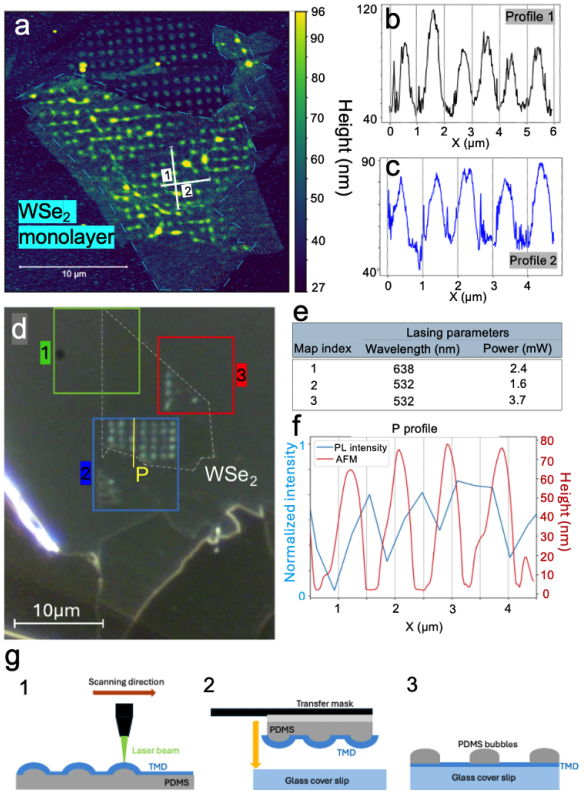

Figure 2: **Nanobubble patterning via laser writing of TMDs on PDMS.** (a) AFM map of the first sample showing 1 µm spacing pattern (b,c). (d) WSe_2 monolayer after laser writing on PDMS with different laser powers and wavelengths and subsequent transfer on glass. (e) Parameters used for the different scans involved in laser writing of the WSe_2 monolayer showed in (d). (f) The same line profile (P in (d)) extracted from the PL map and the AFM map shows how the intensity drops in correspondence of the patterned bubbles. (g) Different phases of the patterning process: laser writing (1), transfer (2) and final result (3).

To test this hypothesis, laser patterning was systematically attempted on both TMD flakes by scanning selected regions while varying the excitation wavelength and laser power (Fig. 2-d,e). The formation of an ordered array of clusters was observed only for scans performed with a 532 nm laser at an optical power of 1.6 mW. In contrast, scans carried out at 2.4 mW using a 638 nm laser left the flakes pristine and flat. These observations suggest the presence of a wavelength threshold between 532 and 638 nm below which the patterning process becomes effective. Similarly, no patterning was observed when using the laser powers typically employed for PL characterization in this work ($\leq$0.16 mW), indicating the existence of a power threshold between 0.16 and 1.6 mW required to induce the patterning process.

Following transfer of the patterned flakes onto glass substrates, PL characterization revealed a local reduction in PL intensity within the patterned regions, without any measurable spectral redshift (Fig. 2-f). The absence of a redshift indicates that no strain is induced in the TMD layer here, suggesting that the patterned clusters are positioned above the TMD after transfer. Consequently, they must have been located beneath the flake during laser exposure on PDMS, as schematically illustrated in Fig. 2-g. This observation suggests that the bubbles are composed of PDMS, which appears to be locally modified upon laser irradiation above specific wavelength and power thresholds.

4. Optical characterization of nanobubbles

Nanobubbles present on one sample were characterized by TEPL (Section 2.2.3) in order to determine the local strain distribution within each bubble. The same sample was subsequently cooled to cryogenic temperatures to investigate the emergence of features compatible with SPE. The strain range associated with bubbles exhibiting such behavior could help to identify the strain conditions under which SPE occurs, with the aim of assessing whether this range corresponds to the regime in which strain-induced hybridization between interband levels, discussed in Section 1.2.2, is expected to take place.

The sample sample was characterized with PL in a temperature range going from 300K down to 15K, before the SPE onset [4].

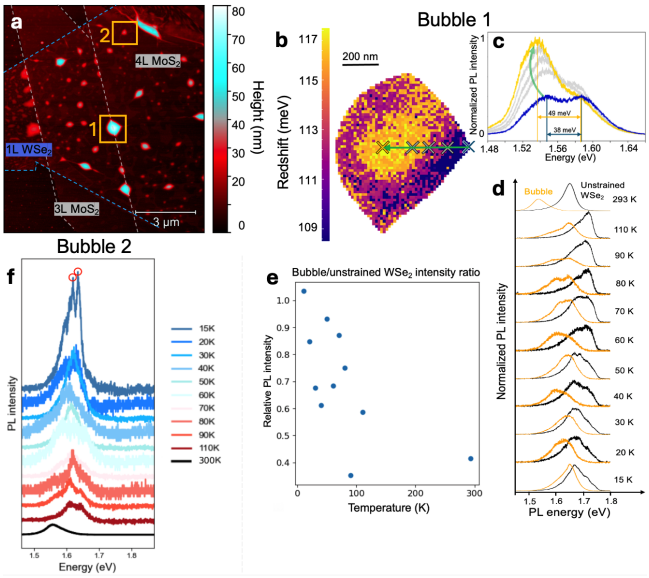

Figure 3: **Optical characterization of Bubbles 1 and 2.** (a) Position of the two bubbles on AFM scan of the sample. (b) TEPL map of Bubble 1. Spectra extracted in different points and marked on the map show strain–driven hybridization occurring (c). (d) T dependency of Bubble 1/unstrained WSe_2 PL intensity ratio. (e) PL spectrum Bubble 1 and free WSe_2 monolayer at different temperatures. (f) PL spectra at different temperatures for Bubble 2.

It is worth to focus in two blisters found in the sample, reported in Fig.3-a and marked as Bubbles 1 and 2. Bubble 1 was characterized by TEPL with a map having 15 nm spacing (Fig.3-b), and showed maximum redshift (i.e. strain) at the center of the bubble. Spectra of the bubble taken at different distances (Fig.3-c) from the center show how the bubble has strain-induced hybridization happening within itself. In fact, at the edge of Bubble 1 the PL shows two distinguishable peaks at 1.59 eV and 1.55 eV, related to splitting of the energy levels obtained after hybridization, and subsequent avoided crossing of the spectra. Approaching inner regions of the bubble, and thus increasing the strain, the lower energy peak becomes more intense, dominating the PL emission at the center of the bubble, and the energetic distance between the two peaks increases. The confocal PL spectra of the same bubble at different temperatures are being plotted together with the spectrum of unstrained WSe_2 1L (Fig.3-d). The ratio in between the bubble and the unstrained WSe_2 intensity maxima was plotted as a function of T (Fig.3-e), showing significant increase approaching lower temperatures, and exceeding 1 at 15 K. Although the increase in intensity at low T is not sufficient to demonstrate SPE, it motivates further investigation at lower temperatures as enhanced brightness under cryogenic conditions above the SPE onset is commonly observed in single–photon sources.
On the other hand, PL characterization on Bubble 2 featured two sharp intense peaks arising in the spectrum at 15 K (Fig.3-f). It is consistent that such spectral features could evolve into quantum emission lines at lower T. The PL peak of Bubble 2 at room T was at 1.56 eV, thus strain-driven hybridization happened at least in part of the blister.

5. Conclusions

This work studied the tunability the average strain and shape of WSe_2 bubbles by varying the adhesion forces between the monolayer and the MoS_2 substrate. This can be done changing the substrate thickness.
Furthermore, a method to deterministically place the bubbles in WSe_2/MoS_2 stacks by laser writing the PDMS support before the transfer was implemented and explored.
Moreover, strain distribution in WSe_2 bubbles was characterized with nanometer resolution, and PL features of strain-driven hybridization were observed within blisters. The PL temperature evolution of those same bubbles led to the observation of signatures consistent with potential SPE occurring upon cooling below 15 K.
Once the strain interval associated with SPE is identified, samples hosting bubbles within this range can be fabricated by selecting an appropriate substrate thickness, as discussed in Section 3.1. Deterministic and reproducible single-photon sources could then be realized following the laser patterning approach described in Section 3.2.

References

[1] T. Björkman, A. Gulans, A. V. Krasheninnikov, and R. M. Nieminen. van der waals bonding in layered compounds from advanced density-functional first-principles calculations. *Phys. Rev. Lett.*, 108:235502, Jun 2012.

[2] Pablo Hernández López, Sebastian Heeg, Christoph Schattauer, Sviatoslav Kovalchuk, Abhijeet Kumar, Douglas J. Bock, Jan N. Kirchhof, Bianca Höfer, Kyrylo Greben, Denis Yagodkin, Lukas Linhart, Florian Libisch, and Kirill I. Bolotin. Strain control of hybridization between dark and localized excitons in a 2d semiconductor. *Nature Communications*, 2022.

[3] Daniel A. Sanchez, Zhaohe Dai, Peng Wang, Arturo Cantu-Chavez, Christopher J. Brennan, Rui Huang, and Nanshu Lu. Mechanics of spontaneously formed nanoblisters trapped by transferred 2d crystals. *Proceedings of the National Academy of Sciences*, 115(31):7884–7889, 2018.

[4] Mikko Turunen, Mauro Brotons-Gisbert, Yunyun Dai, Yadong Wang, Eleanor Scerri, Cristian Bonato, Klaus D. Jöns, Zhipei Sun, and Brian D. Gerardot. Quantum photonics with layered 2d materials. *Nature Reviews Physics*, 2022.

[5] Gang Wang, Alexey Chernikov, Mikhail M. Glazov, Tony F. Heinz, Xavier Marie, Thierry Amand, and Bernhard Urbaszek. Colloquium: Excitons in atomically thin transition metal dichalcogenides. *Rev. Mod. Phys.*, 90:021001, Apr 2018.